




Effect of In addition on microstructure and mechanical properties of Sn–40Bi alloys

Xulei Wu^{1,2} , Jiawei Wu¹, Xiaojing Wang^{1,*}, Jie Yang¹, Ming Xia¹, and Bin Liu^{1,*}

¹School of Material and Science Engineering, Jiangsu University of Science and Technology, Zhenjiang 212003, China

²School of Materials Science and Engineering, Harbin Institute of Technology at Weihai, 2 West Wenhua Road, Weihai 264209, China

Received: 8 May 2019

Accepted: 19 October 2019

Published online:

4 November 2019

© Springer Science+Business Media, LLC, part of Springer Nature 2019

ABSTRACT

The effect of In on melting property, microstructure and mechanical properties of Sn–40Bi– x In ($x = 0, 1, 2, 4, 6, 8$ wt%, respectively) alloys was investigated by means of differential scanning calorimetry, scanning electron microscope, X-ray diffraction and tensile test. The results show that the solidus temperature and the liquidus temperature decrease with the increase in In content. The 1In, 2In and 4In alloys are composed of Sn–Bi eutectic and β -Sn dendrites with In atoms dissolved, whereas 6In and 8In alloys composed of Sn–Bi eutectics, BiIn–Sn metastable phases, Bi particles and primary β -Sn phases. At room temperature, 6In exhibits the maximum ultimate tensile strength of 77 MPa, while 4In displays a more outstanding elongation rate of 42%. Moreover, 2In alloy exhibits an even outstanding elongation behavior (above 300%) at temperatures of 100 and 120 °C.

Introduction

The eutectic Sn–Pb alloy has been widely used in electronic industry. This alloy has many superior properties, such as low cost, good wettability, soldering and a low melting temperature (183 °C) that is suitable for SMT (Surface Mounting Technology) reflow procedure. As increasing concerns on Pb poisoning grow, RoHS (the Restriction of the use of certain Hazardous Substances in electrical and electronic equipment) was introduced in 2001 and set a timeline for eliminating Pb from soldering process 5 years later. The published studies are mainly

focused on alloys Sn–Ag–Cu (SAC) [1–4], Sn–0.7Cu, Sn–8Zn–3Bi [5–8], Sn–58Bi [9, 10] and Sn–42In [11, 12]. When the deadline for implementation of RoHS was approaching in 2006, the leading alternatives to SnPb solder were Sn–3.8Ag–0.7Cu (SAC387) eutectic for reflowing process and SnCu eutectic for waving soldering, both considered acceptable by academia and industry. However, the higher cost of Ag and the patent cost of Iowa University covering SAC eutectic alloy prompted the JEIDA (Japan Electronic Industry Development Association, now JEITA) to endorse the hypoeutectic SAC305 alloy, which was covered by a Japanese patent held by

Address correspondence to E-mail: wxj@just.edu.cn; liubindely@163.com

Senju Metal Industries (patent No. 3027441). SAC 305 performs similar to SAC387 but is much less expensive in price. Therefore, the SAC305 was endorsed as the first choice for product sold to the EU markets promoted by IPC (Association of Connecting Electronics Industries now) and US companies. This resulted in SAC305 largely replacing SAC and SnCu eutectic and activated the database building of SAC305 reliability. Further, the database availability helped SAC305 become the standard Pb-free solder. The cost of SAC305 solder, however, is a concern always due to the high cost of Ag. Under the pressure of competition and the drive of the low cost, reducing Ag content in soldering materials is a choice. As a result, Sn–1.0Ag–0.5Cu (SAC105 for short) [3] and Sn–0.3Ag–0.7Cu [4] have been used as the alternatives for low thermal fatigue and creep requirements. Furthermore, Sn–8Zn–3Bi alloy may have a prospect because of its suitable melting point and bulk properties, which were finally put aside for the short shelf life of the corresponding solder paste using in SMT assembly for the activity of zinc. Similarly, Sn–Bi alloys were no longer suitable to use in electronic industry because of their low mechanical properties and used only in limited applications that did not require much mechanical or thermal performance.

The transition from Sn–Pb to SAC alloys brought many challenges to the packaging procedures and electronics assembly. SAC305 melts between 217 and 221 °C, 34–38 °C higher than the melting point of eutectic Sn–Pb. This melting point increase resulted in the reflowing temperature increase responsively. Consequently, printed circuit boards (PCBs) and electronic components were redesigned to withstand the higher reflow temperatures required by SAC alloys [13]. That was a major inflection point in electronics assembly which brought a great cost rising due to overall adaptability of the production line and the usage of precious metal silver in SAC soldering alloy.

Recent investigations [14, 15] have shown miniaturization of portable electronics and higher package complexity, which drives flip chip BGAs increasingly thinner and the package assembly processes needing multi-steps to finish. Most ultra-thin microprocessors with standard SAC305 alloys result in a great dynamic warpage on package substrate and PCB [14–16]. Such defects can be alleviated, and SMT yields increased when using low-temperature soldering process that reflows below 200 °C [17, 18].

Furthermore, lower reflow temperature enables the usage of cheaper substrates, significantly reducing energy, materials and operational costs, which make it a very compelling proposition. According to road map of iNEMI (International Electronics Manufacturing Initiative) 2015, a lower-temperature soldering technological solution (at least 1–20% lower than the melting temperature of SAC305 alloy) is expected to be achieved within the next 10 years.

Actually, the choice for low-temperature alloys to fulfill SMT (surface mounted technology) soldering requirements is limited. Thus, Sn–8Zn–3Bi, Sn–Bi and Sn–In-based alloys come back under consideration. Sn–8Zn–3Bi alloy needs both alloying technology and upgraded solder paste chemistry to make it possible as a replacement [5–8]. Sn–Bi and Sn–In alloys need more work on the melting properties and mechanical behavior [13].

Based on the previously reported concerning strengthening mechanical performance, it is recognized that the solute content provides a resulting refinement in the microstructural array, i.e., both grain size and dendritic arm spacings [19–22]. And the microstructural array [19–24] is also affected by the cooling rate applied and, consequently, the resulting mechanical behavior can considerably be improved. As for the strengthening of Sn–Bi alloys, the alloying elements are often used to improve mechanical properties and thermal aging resistance through a combination of solid-solution strengthening, precipitate hardening, grain or microstructure refinement and diffusion modifiers [25]. The additive elements such as Ag [9], Al [25, 26], Zn [27, 28], Ni [29], rare earth (RE) [30–32], Cu [33, 34] and In [35] have been verified to be efficient to refine the microstructure and further increase the mechanical properties. Among them, only In addition decreases the melting temperature [35, 37], mainly solutioned into Sn-rich phase [35]. According to the results of Yoon et al. [36], a new Bi–In–Sn metastable phase will be formed when the In content is more than 7 wt%, which may make a different mechanical performance.

Furthermore, decreasing Bi contents from 58 wt% (the eutectic Sn–Bi solder proportion) to 40, 35 and even 17 wt% plus minor silver or copper addition has been verified to be an effective way for meeting step soldering process and relieving the Bi phase segregation along the interface between the substrate and solder alloy [33–35, 38]. And, 40 wt% Bi will be a

better choice which enlarges the solid–liquid region by about 20 °C that meets iNEMI requirement. Furthermore, our previous work [35] and the result of Takao et al. [33] have shown that 40Bi is a better base alloy according to the elongation and UTS.

Therefore, reducing Bi content to 40 wt% with In addition will be an effective way to develop a new low-temperature soldering alloy to meet the urgent needs. In this paper, the melting properties, microstructures and tensile behavior of Sn–40Bi– x In ($x = 0, 1, 2, 4, 6, 8$ wt%, marked as 0In, 1In, 2In, 4In, 6In and 8In, respectively) alloys were systematic investigated.

Experimental procedure

Pure Sn, In and Bi sheets of 99.99 wt% purity were stacked from bottom to top in the center of a 50 mm × 30 mm × 20 mm graphite crucible at room temperature (no In sheet for Sn58Bi alloy), as shown in Fig. 1. Then, the graphite boat was put into a tubular resistance furnace for alloy preparation under the protection of high-purity nitrogen atmosphere at 800 °C for 60 min. The In content in the Sn–40Bi– x In alloy is 0, 1, 2, 4, 6, 8 wt%. A series of alloy ingots were re-melted and stirred at 200 °C for 15 min with an anti-oxidation agent over the surface. Then, the melts were poured into a graphite mold (90 mm ×

90 mm × 20 mm) and cooled in the air to form a plate, which was followed by 2-week aging at room temperature for stabilizing the microstructure. To evaluate the room temperature aging on the change in microstructure, the alloys had been aged for 6 months. Figure 1 shows the preparation procedure of x In alloys.

The microstructure and phase composition of x In alloys were investigated by scanning electron microscopy (SEM, JSM-6480) equipped with energy-dispersive X-ray (EDX) analysis and X-ray diffraction (XRD, RD-6000) analysis. The differential scanning calorimetry (DSC, Pyris Diamond, ± 0.1 °C) measurement was used to analyze the melting temperature of the alloys at a heating rate of 5 °C/min in Ar flow protection of 20 mL/min.

As illustrated in Fig. 2, the dog-bone sample was machined to conduct tensile test with the gauge length of 10 mm, and a rectangle cross section of 1.5 mm × 3 mm. The tests were carried out three times each with a strain rate of 0.01 s⁻¹ under temperatures of 25 °C, 60 °C, 80 °C, 100 °C and 120 °C, respectively. For the tests at elevated temperatures, the tensile specimens were clamped at room temperature and then heated up. Tensile tests were carried out when the temperature reaches the set temperature. After the tensile test, fracture surfaces of specimens were investigated through SEM and EDX.

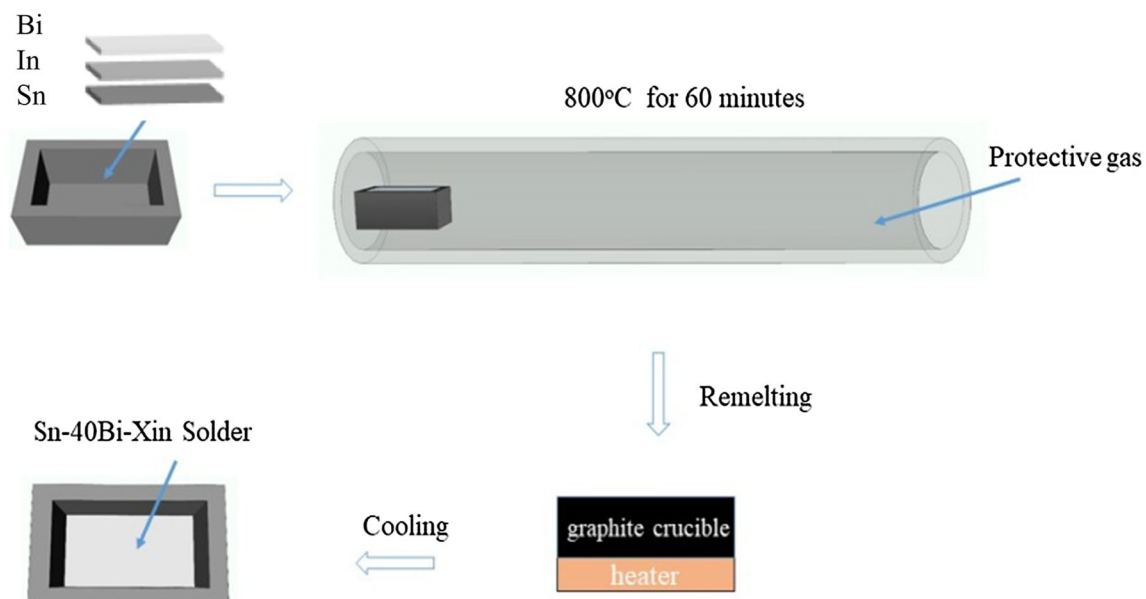


Figure 1 The fabrication procedure of x In alloys (sketch not in scale).

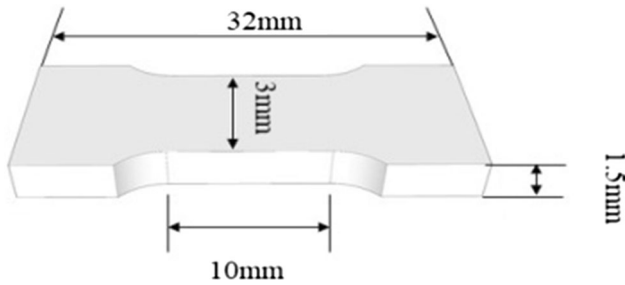


Figure 2 The schematic illustration of tensile test specimen (sketch not in scale).

Results and discussion

Melting properties

Figure 3 shows the DSC curves of x In along with Sn–40Bi alloy upon heating at a scanning rate of 5 °C/min. It is found that when the In content increases from 0 to 8 wt%, the number of exothermal peaks on DSC curves of x In alloy changes from 1 to 4. This peak, marked as peak 1, appears within the temperature range of 137.3–142.9 °C for 0In, 1In and 2In alloys, and 118.9–131.7 °C for 4In, 6In and 8In alloys. Compared with the DSC curves of 0In (Sn–40Bi) and Sn–58Bi alloys in Fig. 3b, Peak 1 should be the heat fluctuation caused by Sn–Bi eutectic phase transformation. This peak shifts slightly from 139.8 °C for 1In alloy to 118.9 °C for 8In alloy. The peak strength decreases with increasing In addition. In other words, In addition depresses the formation of Sn–Bi eutectic phase and enlarges the liquid–solid two-phase region, as shown in Table 1. From this point of view,

the enlarged liquid–solid two-phase zone will make the microstructure of the x In alloy coarser. Also it is noted that the peak temperature of Sn–58Bi eutectic alloy is higher than the generally accepted 138 °C in academic field and 141 °C in industries. The reasons for this distortion may lie in two aspects. Firstly, the curve used in this paper is the heating curve, and secondly, the heating rate is 5 °C/min which is quite high for DSC test. Nevertheless, the purpose of introducing eutectic Sn–58Bi alloy in this work is to provide a ‘reference’ standard to understand the relative melting properties of Sn–40Bi– x In alloys.

However, Sn–40Bi–4In alloy exhibits a different characteristic with a second peak at 136.1 °C indicating a new phase. Further, two more peaks (marked as Peak 3 and Peak 4) arise on the curves of 6In and 8In alloys, indicating the existence of new phases. The XRD patterns of 6In and 8In alloys are presented in Fig. 4. It demonstrates this might be related to BiIn phase.

Generally, the DSC curves also present some other trends besides the above-mentioned peaks with the increasing In content. First, the onset point of Peak 1 decreases from 130.6 to 98.7 °C. Second, the liquidus temperature decreases from 178.2 to 168.2 °C. Third, the peak temperature and phase transformation temperature shift to lower temperature after In addition. Finally, there exists a longer holding time in solid and liquid two-phase zone. The temperatures of four peaks presented in Fig. 3 are listed in Table 1.

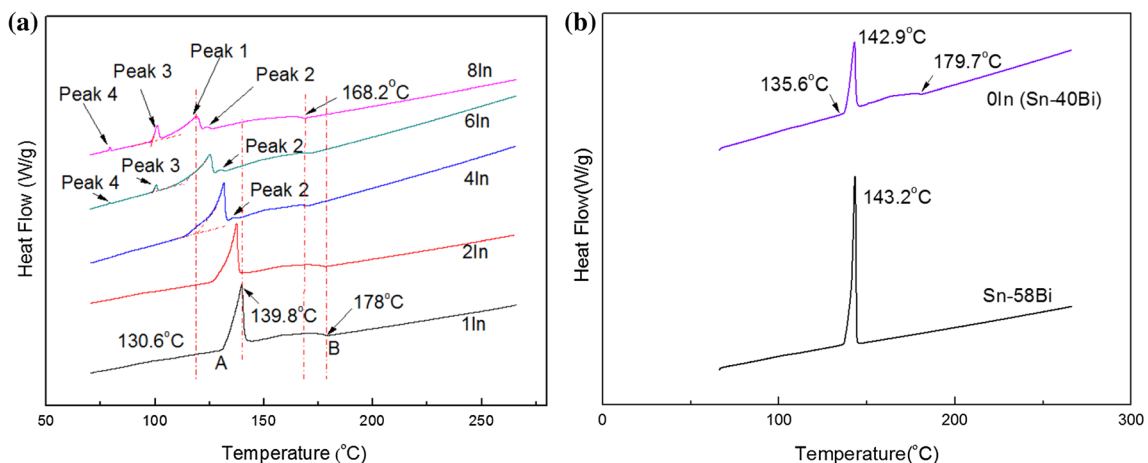
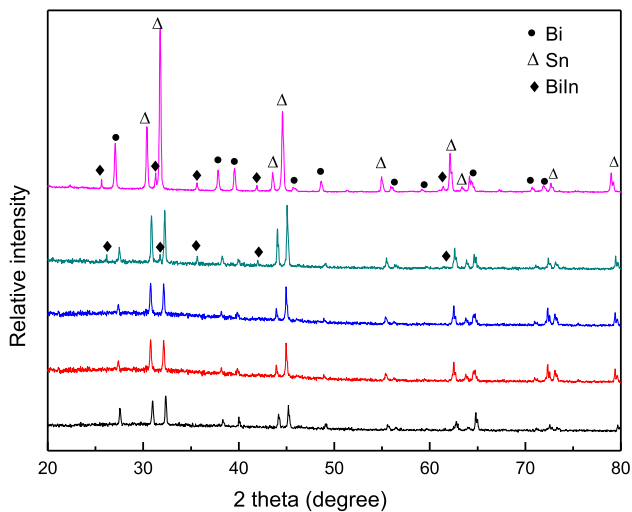


Figure 3 DSC curves of **a** x In alloys ($x = 1, 2, 4, 6, 8$) and **b** 0In (Sn–40Bi) and Sn–58Bi alloys.

Table 1 List of related information shown in Fig. 1 in details

Alloys	Liquidus temperature (°C)	Possible solidus temperature (°C)	Temperature range (°C)	Peak 2 (°C)	Peak 1 (°C)	Peak 3 (°C)	Peak 4 (°C)
Sn–58Bi	143.2	143.2	0		143.2		
0In (Sn–40Bi)	179.7	135.6	44.1		142.9		
1In	178	135.6	47.4		139.8		
2In	178	130.6	51.9		137.3		
4In	169.5	118.5	51	136.1	131.7		
6In	169.5	112 (98.9)	51 (69.3)	129.8	124.9	98.9	79.2
8In	168.2	98.7	69.5	123.8	118.9	98.7	79.2

**Figure 4** XRD patterns of x In alloys ($x = 1, 2, 4, 6, 8$).

Microstructure of x In alloys before and after aging

Microstructure before aging

Figure 5 shows the microstructure of the x In alloys. The bright and dark gray regions represent Bi-rich phase and Sn-rich phase, respectively. The 0In alloy is composed of laminar Sn–Bi eutectic structure and Sn dendrites with Bi particles/strips, as shown in Fig. 5a. The 1In, 2In and 4In alloys show the similar microstructures with 0In alloy except that there are different contents of soluble indium in tin phases and the finer microstructures.

The 6In and 8In alloys are composed of Bi-rich phase, Sn-rich phase and a new phase with white-gray color between the Bi-rich phase and the Sn-rich phase, as shown in Fig. 5e and f. According to the XRD results (Fig. 4) and EDX results (Fig. 5g), the

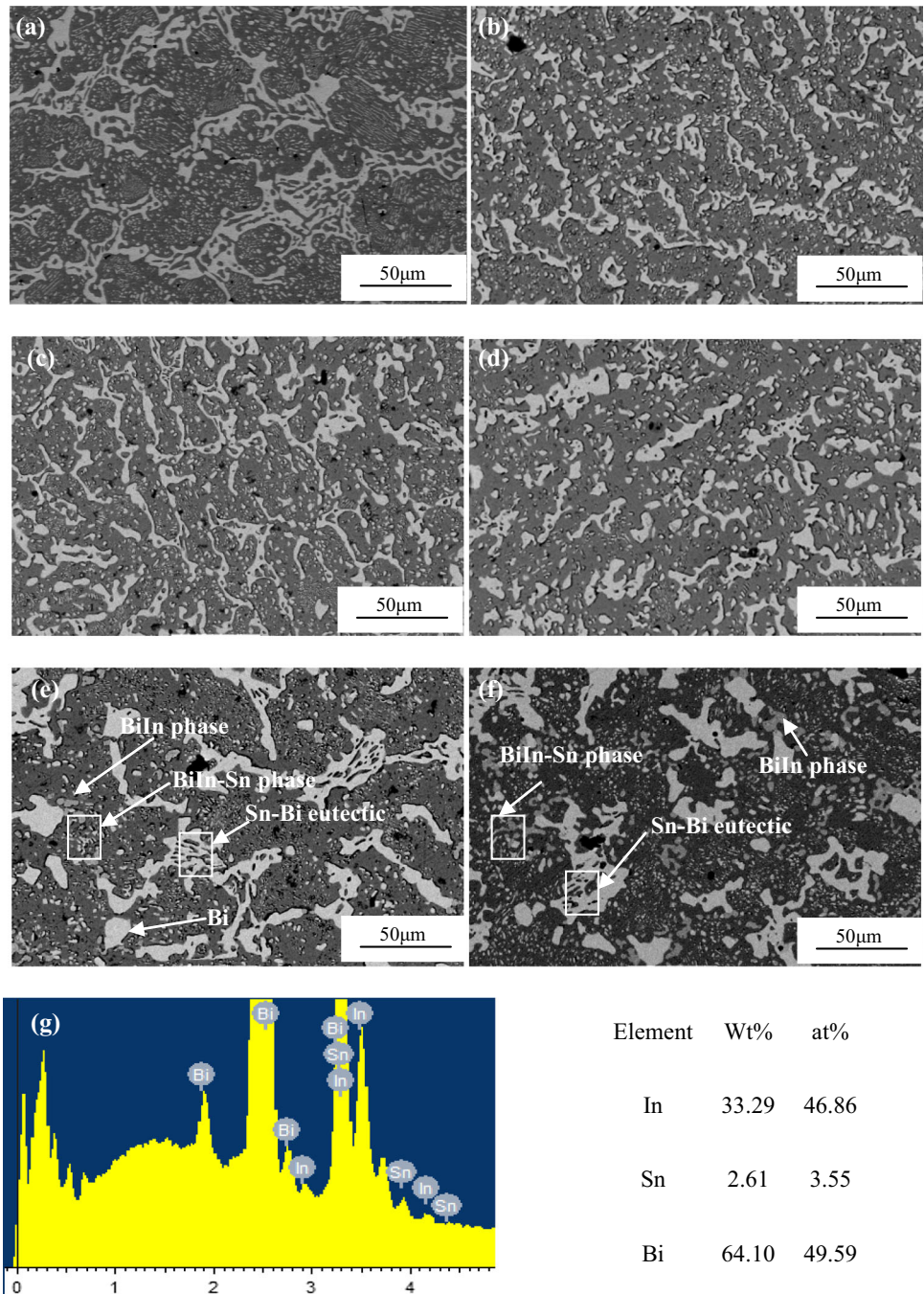
new phase is confirmed to be BiIn phase (PDF number 65-3891). Ruggiero et al. [37] reported that there are several subsystems in Sn–Bi–In system during cooling; a BiIn–Sn metastable phase may be present when the In content is higher. That is, 6In and 8In alloys are composed of Sn–Bi eutectic region, BiIn–Sn coexistence zone, β -Sn and some Bi blocks.

In atoms in 1In, 2In and 4In alloys are completely solid-soluted into Sn-rich phase because the solid-solution phase of In may be Bi-rich phase or Sn-rich phase, or both. For Bi-rich phase, when the content of In is minor the BiIn is the only phase according to the Bi–In phase diagram. For Sn-rich phase, In atoms could completely dissolve in β -Sn lattice because In and β -Sn share a same tetragonal crystal structure due to the similar atom number [39]. The solubility of In in β -Sn is about 9 wt% in equilibrium state [36, 37]. Therefore, it is reasonable to regard the dissolved In in β -Sn at room temperature [35].

As shown in Fig. 5, with In content increasing from 0 to 4 wt%, the Bi-rich phase in eutectic structure first transforms to finer strip, then coarsening when the In content is within the range of 6–8 wt%. This may rely on the following two aspects. First, the addition of In provides more nucleation spots, which leads to the finer microstructure. Second, the addition of In enlarges the solid–liquid two-phase zone and broadens the eutectic transformation peak, which leads to the coarsening of microstructure. As a result, 1–4 wt% In-doped alloys present fine microstructure and 6–8 wt% In-doped alloys appear as a coarse microstructure.

Furthermore, the x In alloys were observed under higher magnified condition with more details shown in Fig. 6. With the increase in In content, Bi phase in eutectic Sn–Bi structure becomes coarsening, which is

Figure 5 Microstructures of a 0In, b 1In, c 2In, d 4In, e 6In, f 8In alloys and g EDX analysis on image.



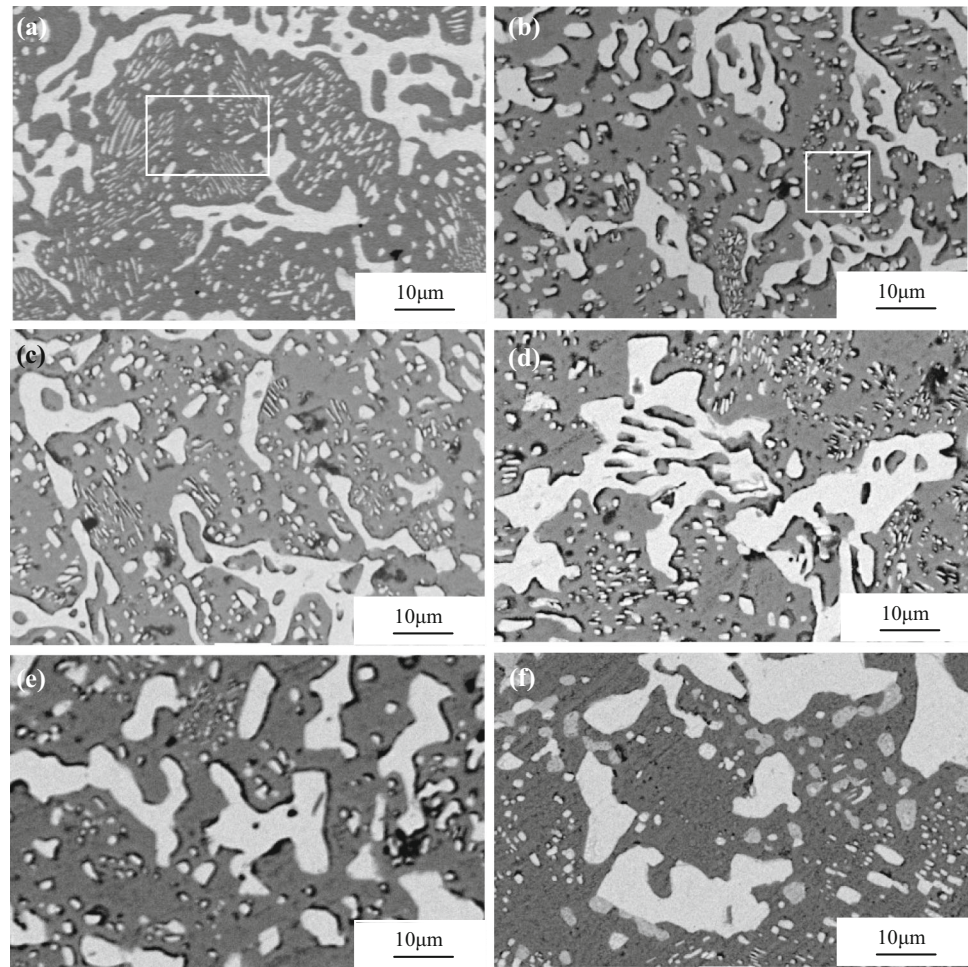
consistent with the widening trend of peak 1. The β -Sn dendrites with rod-like shape in Bi phases with low In content transform to particle shape in highly In-doped alloys. The rod-like structure indicates that this zone during cooling process may experience Bi atom desolvating from the adjacent area in a much stable heat flow field with preferred directions, whereas the particle shape may depend on the

directionless Bi phase growing procedure with more Bi nucleation spots.

Microstructures after room temperature aging

To investigate the structure stability of x In alloys, the microstructure after 6-month room temperature aging was characterized and is shown in Fig. 7. Compared with the previous microstructures, the

Figure 6 Magnified SEM images of **a** 0In, **b** 1In, **c** 2In, **d** 4In, **e** 6In and **f** 8In alloys.



following changes can be clearly observed. Firstly, the Bi particles embedded in β -Sn matrix merge with the Bi phases in Sn–Bi eutectic structure, especially in 1In, 2In and 4In alloys. Secondly, the BiIn–Sn metastable phase zone disappeared and is replaced by bigger BiIn phase embedded in Sn matrix, typically in 6In and 8In solder alloys [36, 37].

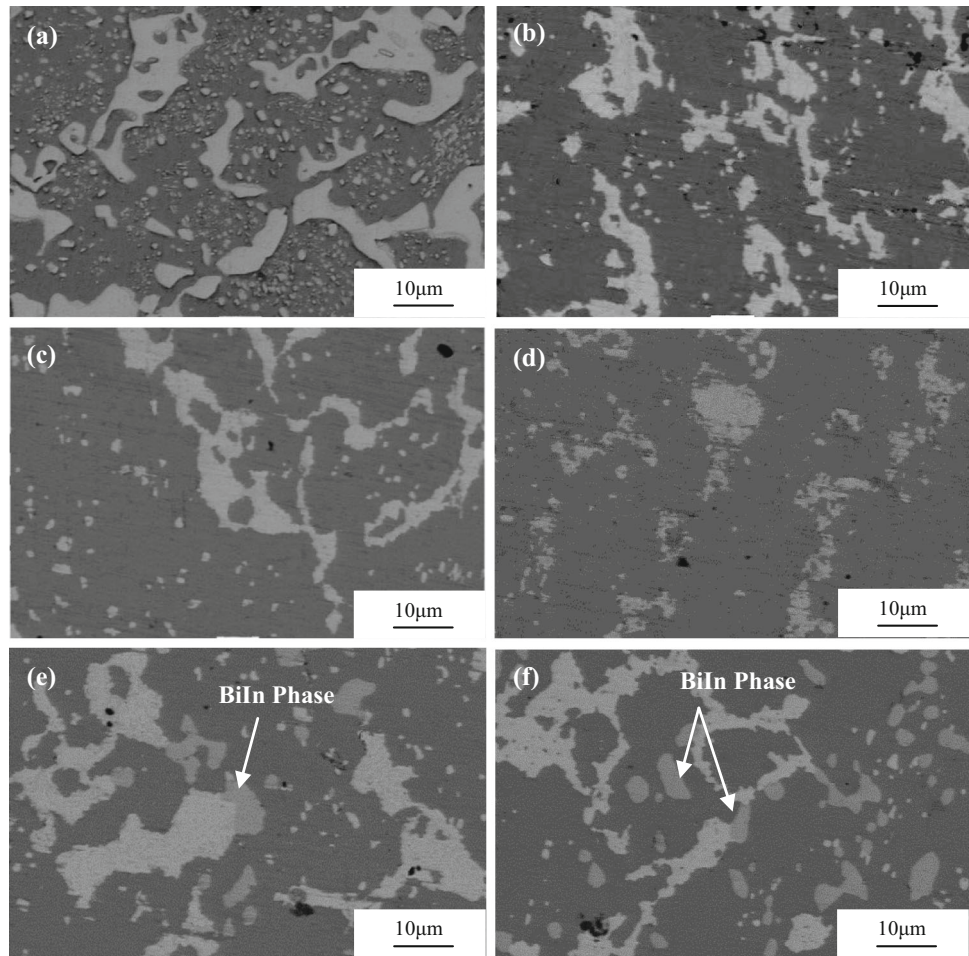
Since the solubility of Bi in Sn is limited, the growth of BiIn particles can be described by the model for the second-phase growth in a saturated solution. The driving force for the growth of BiIn particles is the interface curvature between the two phases. It is called Ostwald ripening. Because the larger particles are much more energetically favored than the smaller ones [40], this originates the fact that molecules on the particle surfaces are energetically less stable than those in the interior. In order to keep the energy to a minimum, molecules on the small-particle surfaces, energetically unfavorable and being with less bonded neighbors, usually tend to depart

from particle surface and solute into the solution. When all the smaller particles disappeared, the concentration of free molecules in solution will increase and finally attain supersaturation. Then, those free molecules tend to solidify on the surface of some larger particles. Thus, all the larger particles grow accompanied by the smaller ones shrinking; and overall the average size of particles increases. Finally, the entire population of particles becomes some large spherical particles to minimize the overall surface area. For the two eutectic phases, namely Sn–Bi and BiIn–Sn, the Sn–Bi phase is more stable.

The possible formation procedure during cooling

In DSC test, the cooling rate is quicker than the equilibrium solidification process. More Bi atoms may dissolve into the primary β -Sn phase. Afterward, Bi particles precipitate from β -Sn phases during cooling with a rod-like structure for Sn matrix

Figure 7 Microstructures of a 0In, b 1In, c 2In, d 4In, e 6In and f 8In alloys after 6-month aging at room temperature.



displaying inner white rectangle frame in Fig. 6a. The solidification process is dependent on the saturation solubility of Bi in β -Sn and the following precipitation behavior. The cooling sequence of phase formation during solidification of the 0In (Sn–40Bi) alloy is as follows: $L \rightarrow L + (\text{primary } \beta\text{-Sn}) \rightarrow \text{SnBi eutectic} + \text{Primary } \beta\text{-Sn} + \text{Bi particles}$ [36, 37, 40–42].

For 1In or 2In alloy, the obtained microstructure shows an enlarged solid + liquid two-phase coexistence zone with 47.4 and 51.9 °C temperature range, respectively. That is, In addition into Sn–40Bi alloy can retard the eutectic transformation. The sequence of phase transformation during cooling is: $L \rightarrow L + (\text{Primary } \beta\text{-Sn}) \rightarrow \text{Eutectic phase transformation} \rightarrow \text{SnBi eutectic} + \text{Primary } \beta\text{-Sn with In dissolved in} + \text{Bi particles}$. The cooling sequence should be similar to Sn–40Bi alloy just with the enlarged solid + liquid zone due to large undercooling.

The 4In alloy shows a wider peak represented by the temperature range in Table 1, 51.9 °C, different from the 44.1 °C of Sn–40Bi alloy, 47.4 °C of 2In alloy,

similar to the 51 °C of 6In alloy. According to the result from Chen et al. [35], BiIn phase will appear when the In content is up to 4 wt%. In this experiment, BiIn phase is not clearly observed in the microstructure and the XRD pattern (Fig. 4). However, the heat release is really large which explains the coarser Bi phase and the nearly invisible eutectic phase in the microstructure (Fig. 6d). The cooling procedure can be regarded as the following: $L_1 \rightarrow L_2 + (\text{Primary } \beta\text{-Sn}) \rightarrow L_3 + \text{Bi} + (\text{Primary } \beta\text{-Sn}) \rightarrow (\text{Sn} + \text{Bi}) \text{ eutectic phase} + \text{Bi} + \text{Primary } \beta\text{-Sn with In dissolved in}$.

According to the DSC curves of alloys 6In and 8In, the phase transformation of the two alloys during cooling should be similar. Based on the results of Yoon et al. [36], there are several independent systems in Sn–Bi–In alloy during cooling, and only one eutectic reaction per independent system possibly occurred. Thus, the eutectic temperature is the lowest phase transition temperature in each independent system. Also previous study from Ruggiero et al. [37]

identifies several eutectic reactions, and they assume that subsystem exists. For instance, they find five eutectic reactions, two from two quasi-binary systems and the three from three subsystems they supposed. During this test condition, it is impossible to reach the theoretical limit uniformity for the liquid phases during cooling process. Thus, using Ruggiero's viewpoint to explain the experimental results is reasonable. As shown in Fig. 8, when 8In alloy is cooled down below 168.2 °C, primary β -Sn phase may precipitate from the liquid. The alloy then enters the liquid + β -Sn two-phase region. Continuous cooling down to 123.8 °C promotes the formation of some extra Bi particles due to the Sn–Bi stoichiometric reaction. When the temperature is around 118.9 °C, the appearing peak is similar to the other peak 1 shifted to the lower temperature, representing Sn–Bi

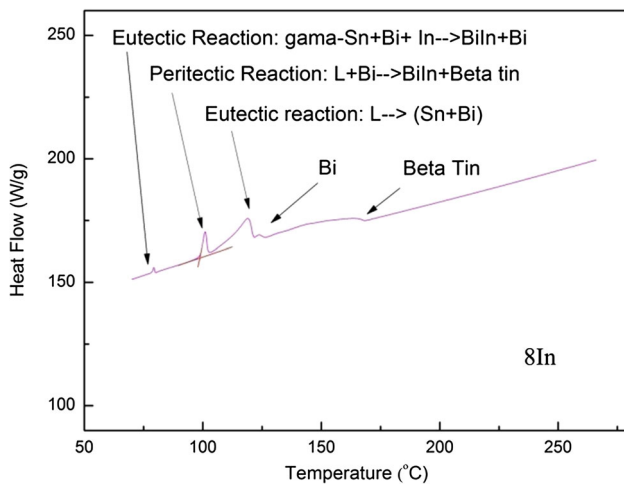


Figure 8 DSC curve of 8In alloy.

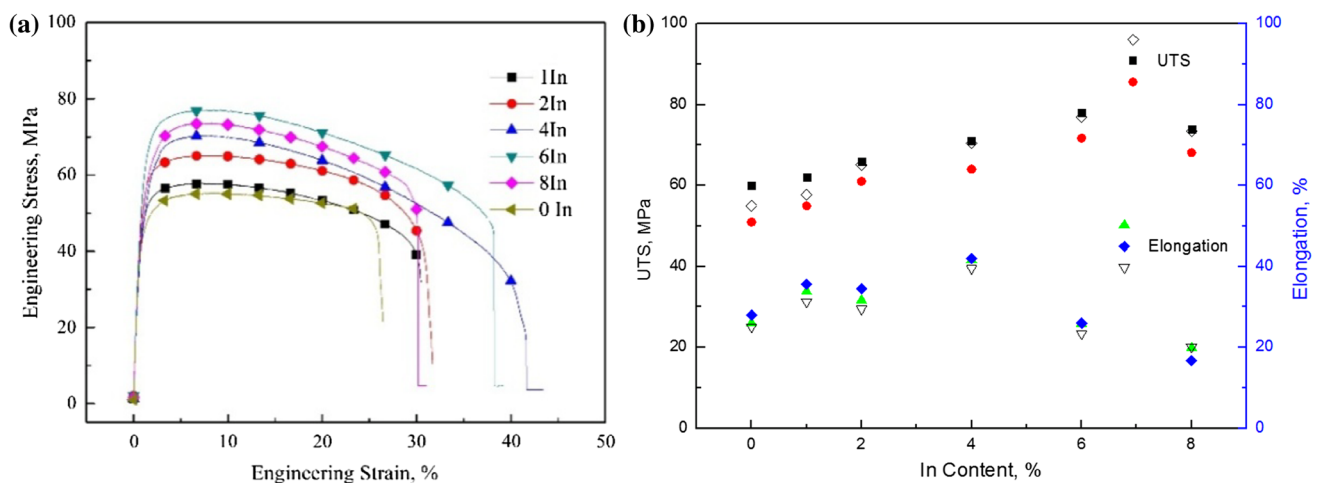


Figure 9 x In alloys ($x = 0, 1, 2, 4, 6, 8$) under tensile test: **a** stress–strain curves and **b** In addition versus UTS and Elongation.

eutectic transformation. That is verified by Sn–Bi eutectic zones in 6In and 8In alloys shown in Fig. 4d and f. After temperature is lower than 98.7 °C, most of the residue liquid may transform to BiIn + Bi phase, replacing the area that is previously occupied by $(L + \text{BiIn} + \beta\text{-Sn})$ and $(L + \text{BiIn} + \text{Bi})$. The $(L + \text{BiIn} + \beta\text{-Sn})$ phase field keeps until it reaches the next reaction, occurring at 79.2 °C [43]. Thus, the reaction at 98.7 °C can be expressed as $L + \text{Bi} \rightarrow \beta\text{-Sn} + \text{BiIn}$. The last minor peak may be represented by the reaction of $L \rightarrow$ eutectic BiIn–Sn phase. Thus, the whole cooling sequence can be expressed by the following series of processes: $L \rightarrow L_1 + (\text{primary } \beta\text{-Sn}) \rightarrow L_2 + \text{Bi} + (\text{primary } \beta\text{-Sn}) \rightarrow L_3 + \text{eutectic (Sn + Bi)} + \text{Bi} + (\text{primary } \beta\text{-Sn}) \rightarrow L_4 + (\beta\text{-Sn} + \text{BiIn}) + \text{eutectic (Sn + Bi)} + (\text{primary } \beta\text{-Sn}) + \text{Bi} \rightarrow \text{BiIn-Sn} + (\beta\text{-Sn} + \text{BiIn}) + \text{eutectic (Sn + Bi)} + (\text{primary } \beta\text{-Sn}) + \text{Bi} \rightarrow$ final room temperature: $\beta\text{-Sn} + \text{BiIn} + \text{Bi}$.

Tensile properties

Tensile properties at room temperature

The tensile properties of x In alloys in room temperature were investigated. The stress–strain curves obtained from tensile tests are shown in Fig. 9a. The relationship between the ultimate tensile strength (UTS) and elongation rate with In content is shown in Fig. 9b. The 6In alloy displays a maximal UTS of 77 MPa, whereas 4In alloy gives the best elongation of 42%. This might be owing to the distribution of element In changes from solid solution in β -tin base to BiIn–Sn metastable phase (BiIn phase finally) and

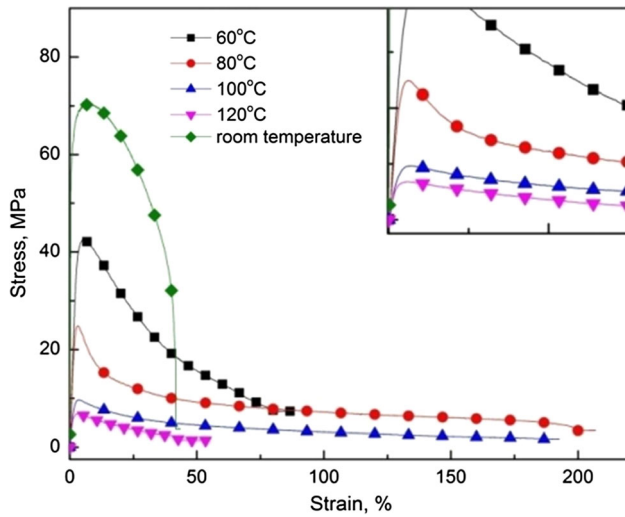
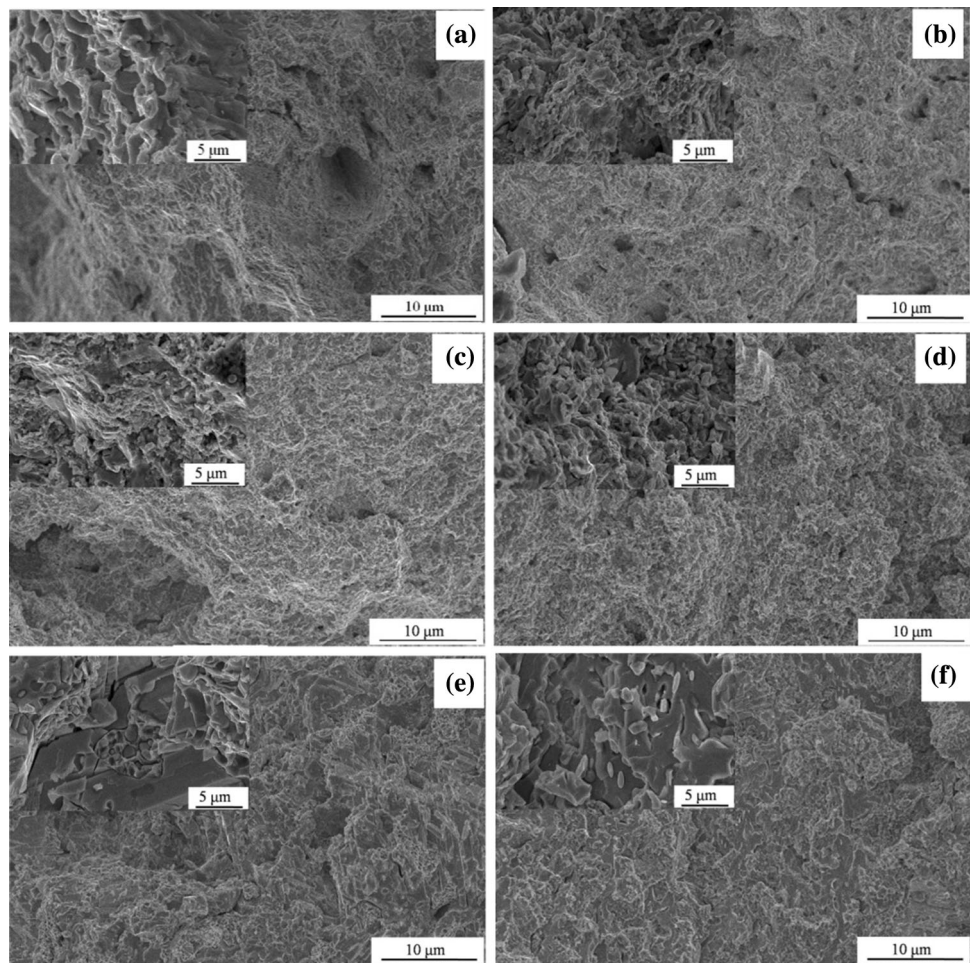


Figure 10 Stress–strain curves of 4In alloy at room temperature, 60 °C, 80 °C, 100 °C and 120 °C (inset top right is local magnified image correspondingly).

the coarsening of eutectic zone with Bi content increasing. Shalaby et al. [44] investigated the creep behavior of Bi–Sn alloy and found that the extra Bi could strengthen β -Sn phase, which was further counteracted by the softening effect of In addition. As shown in Fig. 5, it finds that with In addition, Bi phase coarsens. According to Chen et al. [35], 2.5 wt% In-doped Sn–Bi alloy exhibits remarkable elongation behavior. In this paper, 4 wt% In-doped Sn–Bi alloy displays the maximum elongation rate. This difference might be due to the different microstructures of the two works. The as-cast x In ingot has been aged for 2 weeks in this study which may stimulate the supersaturated Bi atoms precipitate from the beta tin base. The aging softens In-containing alloys and further improves the ductile properties, while the BiIn phase formation worsens plastic performance.

As shown in Fig. 9, the elastic modulus of x In alloy is basically the same. The value is mainly related to

Figure 11 Fracture morphologies of (inset top left is magnified image correspondingly): a 0In, b 1In, c 2In, d 4In, e 6In and f 8In alloys at room temperature.



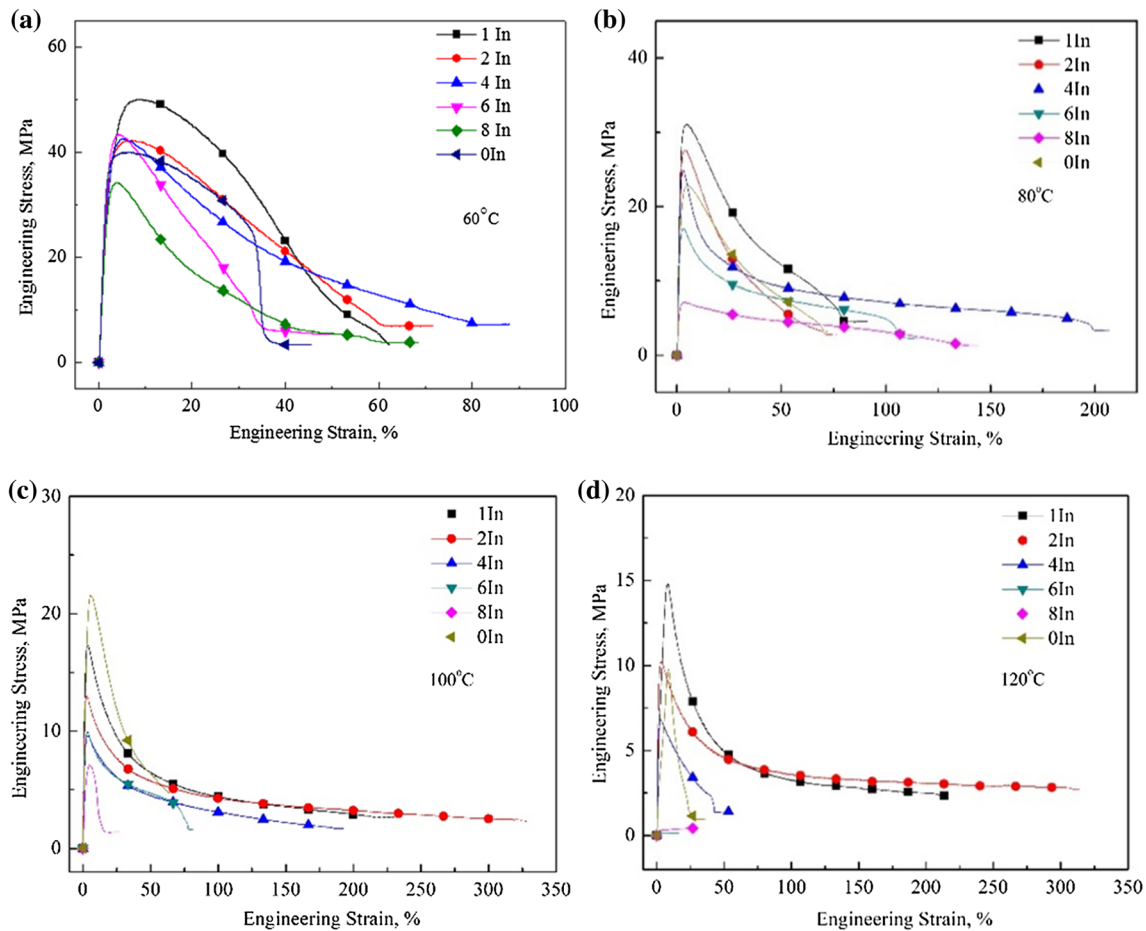


Figure 12 Stress–strain curves of $x\text{In}$ ($x = 0, 1, 2, 4, 6, 8$) alloys at **a** 60 °C, **b** 80 °C, **c** 100 °C and **d** 120 °C.

atomic bonds which are insensitive to the microstructure and therefore to the different $x\text{In}$ alloys; they are very temperature dependent. When the temperature increases, the elastic modulus decreases, as shown in Fig. 10.

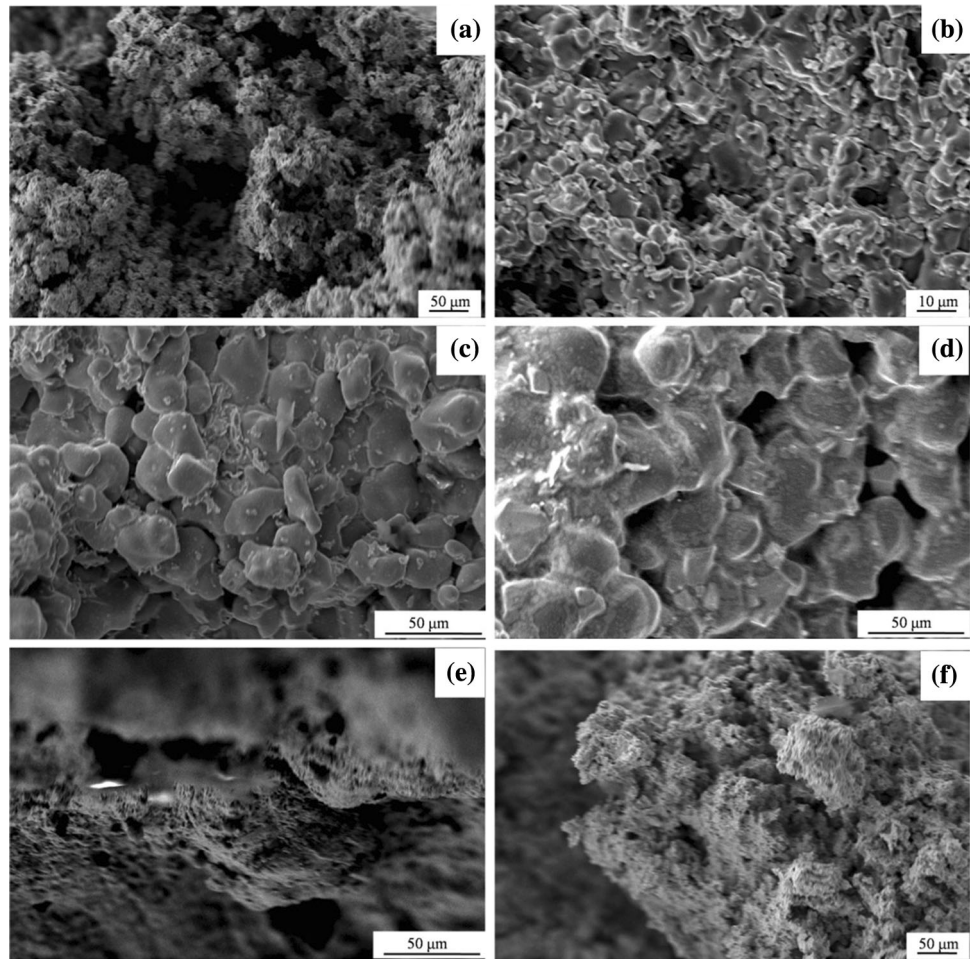
Figure 11 demonstrates the fracture morphologies of $x\text{In}$ alloys. It shows all alloys exhibit ductile fractures. However, the dimples can only be seen on the fracture surfaces of 0In, 1In, 2In and 4In alloys. The fracture surfaces of 6In and 8In alloys are relatively flat in general and exhibit some cleavage feature in high-magnified images, which is consistent with the elongation results.

Tensile properties at high temperatures

Figure 12 shows the stress–strain curves of $x\text{In}$ alloys at high temperatures of 60, 80, 100 and 120 °C, respectively. It is found that UTS of all the tested alloys decrease with the increase in In content. It is

also noticed that the 4In alloy holds the maximum fracture strain at temperatures of 60 and 80 °C. The fracture strain of 4In alloy can even exceed 200% at temperature of 80 °C. The UTS of 2In alloy is maximum at temperature of 100 °C, but 1In alloy holds the maximum UTS when the temperature is further increased to 120 °C. The 2In alloy holds the maximum fracture strain at temperature of 100 and 120 °C, and the value of maximum fracture strain is 327% and 313%, respectively. The reason for this phenomenon may relate to the addition of In. In addition, the shape of tensile curve changes from dome-like shape at low temperature to sharp peak appearance at high temperature. Take the tensile curves at 120 °C as an example, 6In and 8In alloys almost lost the ability to resist the external loading process. This is no doubt that it is due to the existence of low-melting-point phase, based on the previous DSC analysis, which could be a reason for the strength decay.

Figure 13 Fracture surfaces of **a** 0In, **b** 1In, **c** 2In, **d** 4In, **e** 6In and **f** 8In alloys after tensile tests at 120 °C.



As shown in Fig. 13, the tensile fracture of x In alloys at 120 °C exhibits ductile fracture, but the fracture morphology is different from that at room temperature. The fracture surface of 0In alloy becomes rougher showing a better ductile property, as shown in Fig. 13a. The fracture morphologies of 1In, 2In and 4In alloys are flat and smooth covered by the round particles. The particles sizes are 5–10 μm for 1In alloy, 25 μm for 2In alloy and about 50 μm for 4In alloy. These particles are Sn-rich and Bi-rich phases according to the previous microstructure observation. The 1–4 wt% In addition induces the Sn and Bi phase boundary to slide easily at 120 °C. And the phase boundary sliding should be the main source of superior plasticity of 1In and 2In alloys. For the fracture of 4In alloy, the surface of particles becomes rough, which leads to the relatively lower fracture strain compared with 1In and 2In alloys. Further, the fracture surfaces of 6In and 8In alloys look like totally collapsing after tensile test at a temperature of 120 °C.

Conclusion

The effects of In addition on the melting properties, microstructures and mechanical responses of Sn–40Bi alloy were investigated. The conclusions can be drawn as follows:

1. When the content of In is in the range of 1–8 wt%, the DSC curve shows that the peak of thermal fluctuation of the alloy during heating or cooling is from one peak of 1In alloy to four peaks of 8In alloy. And the indium addition makes all the phase transformation temperatures of Sn–40Bi alloy move toward lower temperature.
2. The phase transformation sequence for 8In alloy can be written as : $L \rightarrow L_1 + (\text{primary } \beta\text{-Sn}) \rightarrow L_2 + \text{Bi} + (\text{primary } \beta\text{-Sn}) \rightarrow L_3 + \text{eutectic (Sn + Bi)} + \text{Bi} + (\text{primary } \beta\text{-Sn}) \rightarrow L_4 + (\beta\text{-Sn} + \text{BiIn}) + \text{eutectic (Sn + Bi)} + (\text{primary } \beta\text{-Sn}) + \text{Bi} \rightarrow \text{BiIn-Sn} + (\beta\text{-Sn} + \text{BiIn}) + \text{eutectic}$

(Sn + Bi) + (primary β -Sn) + Bi \rightarrow final room temperature: β -Sn + BiIn + Bi.

3. The microstructures for 1In, 2In and 4In alloys are arranged by β -Sn dendrites with In dissolved in, Bi precipitates with uniform distribution and a complex eutectic mixture. The 6In and 8In alloys present a different initial microstructure composed of Sn-Bi eutectic, BiIn-Sn metastable phase, Bi particles and β -Sn matrix, which finally evolves into a more stable structure of β -Sn, BiIn and Bi phases.
4. At room temperature, the UTS and fracture strain of the alloy increase first and then decrease with the increase in In content. This trend is caused by the transformation of In existence from solid solution in β -Sn of 1In, 2In and 4In alloys to BiIn-Sn metastable phase or BiIn phase of 6In and 8In alloys. And 6In exhibits a much higher ultimate tensile strength (UTS) of 77 MPa, while 4In displays a more outstanding elongation rate of 42%. When the tensile tests were taken at 60, 80, 100 and 120 °C separately, the UTS decreases with the increase in temperature. 2In alloy instead of 4In alloy displays the maximum elongation rate over 300% at 100 and 120 °C.

Acknowledgements

This work was supported by the National Natural Science Foundation of China (Grant Nos. 51541104, 51402132) and Jiangsu Planning Project of Science and Technology (Grant No. BK20150466).

References

- [1] Wang XJ, Zeng QL, Zhu QS, Wang ZG, Shang JK (2010) Effects of current stressing on shear properties of Sn-3.8Ag-0.7Cu solder joints. *J Mater Sci Technol* 26(8):737–742
- [2] Wang JX, Nishikawa H (2014) Impact strength of Sn-3.0Ag-0.5Cu solder bumps during isothermal aging. *J Microelectron Reliab* 54(8):1583–1591
- [3] Cheng F, Gao F, Zhang J, Jin W, Xiao X (2011) Tensile properties and wettability of SAC0307 and SAC105 low Ag lead-free solder alloys. *J Mater Sci* 46:3424–3429. <https://doi.org/10.1007/s10853-010-5231-8>
- [4] Kanlayasiri K, Sukpimai K (2016) Effects of indium on the intermetallic layer between low-Ag SAC0307-xIn lead-free solders and Cu substrate. *J Alloys Compd* 668(25):169–175
- [5] Ren G, Collins MN (2017) The effects of antimony additions on microstructures, thermal and mechanical properties of Sn-8Zn-3Bi alloys. *J Mater Des* 119:133–140
- [6] Billah MM, Shorowordi KM, Sharif A (2014) Effect of micron size Ni particle addition in Sn-8Zn-3Bi lead-free solder alloy on the microstructure, thermal and mechanical properties. *J Alloys Compd* 585:32–39
- [7] Ren G, Wilding IJ, Collins MN (2016) Alloying influences on low melt temperature SnZn and SnBi solder alloys for electronic interconnections. *J. Alloys Compd* 665:251–260
- [8] Ren G, Collins MN (2019) On the mechanism of Sn tunnelling induced intermetallic formation between Sn-8Zn-3Bi solder alloys and Cu substrates. *J Alloys Compd* 791:559–566
- [9] Ren G, Collins MN (2019) Improved reliability and mechanical performance of Ag microalloyed Sn58Bi solder alloys. *Metals* 29(4):462
- [10] Zuo Y, Ma L, Liu S, Wang T, Guo F, Wang X (2013) The coupling effects of thermal cycling and high current density on Sn58Bi solder joints. *J Mater Sci* 48(6):2318–2325. <https://doi.org/10.1007/s10853-012-7011-0>
- [11] Tian F, Shang PJ, Liu ZQ (2014) Precise Cr-marker investigation on the reactive interface in the eutectic SnIn solder joint. *J Mater Lett* 121(15):185–187
- [12] Tian F, Liu ZQ, Shang PJ, Guo JD (2014) Phase identification on the intermetallic compound formed between eutectic SnIn solder and single crystalline Cu substrate. *J Alloys Compd* 591(5):351–355
- [13] Ribas M, Hunsinger T, Cucu T, Ramakrishna HV, Lim G, Murphy M (2018) The printed circuit assembler's guide to low-temperature soldering. BR Publishing, Inc., New Delhi
- [14] Aspandiar R, Byrd K, Tang KK, Campbell L, Mokler S (2015) Investigation of low-temperature solders to reduce reflow temperature, improve SMT yields and realize energy savings. IPC APEX EXPO, San Diego, California. February
- [15] Wang K, Wang F, Huang Y, Qi K (2019) Comprehensive properties of a novel quaternary Sn-Bi-Sb-Ag solder: wettability, interfacial structure and mechanical properties. *Metals* 9(7):791
- [16] Chen OH, Molina A, Aspandiar R, Byrd K, Mokler S, Tang KK (2015) Mechanical shock and drop reliability evaluation of the BGA solder joint stack-ups formed by reflow soldering SAC solder balls BGAs with BiSnAg and resin reinforced BiSn-Based solder pastes. In: SMTA international conference and exhibition. Rosemont, Illinois. September
- [17] Sidhu RS, Renavikar MP, Dani AA, Dudek MA (2014) Solder paste material technology for elimination of high warpage surface mount assembly defects. U.S. Patent, 0175160 A1

- [18] Mokler S, Aspandiar R, Byrd K, Chen O, Walwadkar S, Tang KK, Renavikar M, Sane S (2016) The application of Bi-based solders for low-temperature reflow to reduce cost while improving SMT yields in client computing systems. In: SMTA international conference and exhibition, Rosemont, Illinois. September
- [19] Garcia LR, Peixoto LC, Osorio WR, Garcia A (2009) Globular-to-needle Zn-rich phase transition during transient solidification of a eutectic Sn-9%Zn solder alloy. *J Mater Lett* 63:1314–1316
- [20] Garcia LR, Osório WR, Garcia A (2011) The effect of cooling rate on the dendritic spacing and morphology of AgSn intermetallic particles of a SnAg solder alloy. *J Mater Des* 32:3008–3012
- [21] Çadırılı R, Kaya H, Boyuk U, Maraşlı N (2012) Effect of solidification parameters on the microstructure of directionally solidified Sn–Bi–Zn lead-free solder. *J Met Mater Int* 18:349–354
- [22] Zhang C, Liu SD, Qian GT, Zhou J, Xue F (2014) Effect of Sb content on properties of Sn–Bi solders. *J Trans Nonferrous Met Soc China* 24(1):184–191
- [23] Liu JC, Wang ZH, Xie JY, Ma JS, Shi QY, Zhang G, Suganuma K (2016) Effects of intermetallic-forming element additions on microstructure and corrosion behavior of Sn–Zn solder alloys. *J Corrosion Sci* 112:150–159
- [24] Lai Z, Ye D (2016) Microstructure and fracture behavior of non eutectic Sn–Bi solder alloys. *J Mater Sci: Mater Electron* 27:1–10
- [25] Chen Y, Wu XL, Wang XJ, Huang H (2016) Effects of reflow time on the interfacial microstructure and shear behavior of the SAC/FeNi–Cu joint. *Metals* 6(5):109
- [26] Wang XJ, Zhu QS, Liu B, Liu N, Wang FJ (2014) Effect of doping Al on the liquid oxidation of Sn–Bi–Zn solder. *J Mater Sci: Mater Electron* 25:2297–2304
- [27] Wang XJ, Wang YL, Wang FJ, Liu N, Wang JX (2014) Effects of Zn, Zn–Al and Zn–P additions on the tensile properties of Sn–Bi solder. *J Acta Metall Sin (Engl Lett)* 27(6):1159–1164
- [28] Wang FJ, Chen H, Huang Y, Liu LT, Zhang Z (2019) Recent progress on the development of Sn–Bi based low-temperature Pb-free solders. *J Mater Sci: Mater Electron* 30:3222–3243
- [29] Mokhtari O, Nishikawa H (2016) Correlation between microstructure and mechanical properties of Sn–Bi–X solders. *J Mater Sci Eng A* 651:831–839
- [30] Wang JX, Xue SB, Han ZJ, Yu SL, Chen Y, Shi YP, Wang H (2009) Effects of rare earth Ce on microstructures, solderability of Sn–Ag–Cu and Sn–Cu–Ni solders as well as mechanical properties of soldered joints. *J Alloys Compd* 467(1–2):219
- [31] Wu C, Shen J, Peng C (2012) Effects of trace amounts of rare earth additions on the microstructures and interfacial reactions of Sn57Bi1Ag/Cu solder joints. *J Mater Sci: Mater Electron* 23(1):14–21
- [32] Dong WX, Shi YW, Xia ZD, Lei YP, Guo F (2008) Effects of trace amounts of rare earth additions on microstructure and properties of Sn–Bi-based solder alloy. *J Electron Mater* 37(7):982–991
- [33] Takao H, Yamada A, Hasegawa H (2004) Mechanical properties and solder joint reliability of low-melting Sn–Bi–Cu lead free solder alloy. *R&D Rev Toyota CRDL* 39(2):41
- [34] Wu XL, Xia M, Li SJ, Wang XJ, Liu B, Zhang JX, Liu N (2017) Microstructure and mechanical behavior of Sn–40Bi–x Cu alloy. *J Mater Sci: Mater Electron* 28(20):15708–15717
- [35] Chen X, Xue F, Zhou J, Yao Y (2015) Effect of In on microstructure, thermodynamic characteristic and mechanical properties of Sn–Bi based lead-free solder. *J Alloys Compd* 633:377
- [36] Yoon SW, Rho B, Lee HM, Kim C, Lee BJ (1999) *J Metall Mater Trans A* 30(6):1503–1515
- [37] Ruggiero MA, Rutter JW (1995) Origin of microstructure in 350 K eutectic of Bi–In–Sn ternary system. *J Mater Sci Technol* 11:136–142
- [38] Shen J, Wu C, Li S (2012) Effects of rare earth additions on the microstructural evolution and microhardness of Sn30Bi0.5Cu and Sn35Bi1Ag solder alloys. *J Mater Sci: Mater Electron* 23:156–163
- [39] Santos WLR, Brito C, Bertelli F, Spinelli JE, Garcia A (2015) Microstructural development of hypoeutectic Zn–(10–40)wt%Sn solder alloys and impacts of interphase spacing and macrosegregation pattern on hardness. *J Alloys Compd* 647:989
- [40] Ratke L, Voorhees PW (2002) Growth and coarsening: Ostwald ripening in material processing. Springer, Berlin, p 117
- [41] Witusiewicz VT, Hecht U, Bottger B, Rex S (2007) Thermodynamic re-optimisation of the Bi–In–Sn system based on new experimental data. *J Alloys Compd* 428(1–2):115–124
- [42] Li Q, Ma N, Lei YP, Lin J, Fu HG, Gu J (2016) Characterization of low-melting-point Sn–Bi–In lead-free solders. *J Electron Mater* 45(11):5800–5810
- [43] Kanlayasiria K, Mongkolwongrojnb M, Arigac T (2009) Influence of indium addition on characteristics of Sn–0.3Ag–0.7Cu solder alloy. *J Alloys Compd* 485(1–2):225

- [44] Shalaby RM (2013) Effect of silver and indium addition on mechanical properties and indentation creep behavior of rapidly solidified Bi–Sn based lead-free solder alloys. *J Mater Sci Eng: A* 560:86–95

Publisher's Note Springer Nature remains neutral with regard to jurisdictional claims in published maps and institutional affiliations.